Jointing analysis of scATAC-seq datasets using epiConv

Li Lin[1*], Liye Zhang[1*]

[1]School of Life Science and Technology, ShanghaiTech University, Shanghai, China.

[*]Correspondence should be addressed to L.L. (linli@shanghaitech.edu.cn) or L.Z. (zhangly@shanghaitech.edu.cn).

Abstract

Technical improvement in ATAC-seq makes it possible to profile the chromatin states of single cells at high throughput, but currently no method is available to integrate datasets from multiple sources (different batches of same protocol or multiple experimental protocols). Here we present an algorithm to perform joint analyses on scATAC-seq datasets from multiple sources. In addition to batch correction, we also demonstrate that epiConv is capable of aligning co-assay data (simultaneous profiling of transcriptome and chromatin) onto high-quality ATAC-seq reference or integrating cells in different biological conditions (malignant *vs.* normal), which increases the statistical power of downstream analyses and reveals hidden hierarchy of malignant cells.

Text

The expression of genes is regulated by transcription factors (TFs) that bind to the regulatory elements of the genome. As the accessible chromatin covers more than 90% TF binding regions, many techniques, such as Assay for Transposase-Accessible Chromatin using sequencing (ATAC-seq), have been developed to detect accessible chromatin[1-3]. Recent technical advancements have made it possible to profile the chromatin states of single cells at a high-throughput manner and along with other molecular modalities (e.g. transcriptome) in the same cells[4-6]. Similar to RNA-seq, ATAC-seq data also suffers from batch effects[7]. But batch correction on scATAC-seq data is more challenging as it is difficult to capture and correct batch derived variations on nearly binary chromatin profiles. For now, there are no specialized batch correction tool designed for scATAC-seq data to our knowledge. Most clustering algorithms for scATAC-seq data capture biological information by learning a series of latent features from binary chromatin profiles. But whether latent features are confounded by batch effects and most importantly, whether batch effects can be removed by scaling these latent features by conventional ways used in scRNA-seq analysis, remain unclear.

Here, we develop a novel algorithm named epiConv (https://github.com/LiLin-biosoft/epiConv) for joint analysis of scATAC-seq data. EpiConv learns the similarities between cells by directly comparing their chromatin profiles (the dot product of two vectors of cells and followed by subsequent library size normalization) (**Fig. 1a**). Comparing to existing algorithms, epiConv performs similarly or slightly better on clustering and embedding (**Fig. S1**). However, its most significant advantage over other methods is that epiConv introduces an additional procedure to remove batch related bias in joint analysis of multiple datasets (**Fig. 1b**): it captures

41 batch derived variations by Eigenvalue Decomposition and remove them by properly scaling the
42 Eigen vectors (See method section for more details). Through comprehensive benchmarking, we
43 demonstrated that epiConv was capable of removing batch effects and in the meantime retaining
44 biological signals.

45 We first applied epiConv to a collection of peripheral blood mononuclear cells (PBMCs)
46 datasets from two studies sequenced by two protocols (10x Genomics and dscATAC-seq) to
47 benchmark its performance of batch correction[5, 8]. For comparison, we also applied two
48 commonly used clustering algorithms of scATAC-seq data (cisTopic[9] and Latent Sematic Indexing[4],
49 LSI) to calculate a set of latent features and then removed the batch effects by scaling the latent
50 features using Harmony[10] (batch correction algorithm developed for scRNA-seq). Without batch
51 correction, all three methods (epiConv, cisTopic and LSI) exhibited obvious batch effects between
52 two studies (**Fig. 1c**). After batch correction, epiConv mixed single cells from two studies together,
53 while cells were still partially or completely clustered by their data source in other methods (**Fig.**
54 **1c**). In order to quantitatively evaluate the performance of batch correction, we calculated the
55 information entropy of batch mixing among each cell's nearest neighbors. EpiConv showed
56 significant improvements of information entropy over other methods, which suggested that
57 epiConv better mixed cells from multiple datasets together (**Fig. 1d**). To evaluate whether cells
58 were grouped based on their biological identities, we performed differential analysis on single
59 cells with known biological identities to get a set of marker chromatin regions for each known cell
60 type. Given that CD8+ T cells grouped into two distinct clusters (naïve CD8+ cluster with
61 accessible *CCR7* promoter and effecter CD8+ cluster with accessible *CCL5* promoter), we
62 performed differential analysis to get markers for both naïve and effector CD8+ clusters. We

63 summed the number of accessible peaks among these markers in single cells to calculate meta
64 signatures that represented their similarities to known cell types. For each cell type, cells with
65 high signature scores from two studies were grouped together and along with the corresponding
66 cells with known identities (compare **Fig. S2** with **Fig1c**), suggesting that epiConv retained
67 biological heterogeneity.

68 EpiConv can also increase the resolution of chromatin profiles through joint analysis. Next,
69 we demonstrated that aligning the ATAC-seq profiles of co-assay data (perform scRNA-seq and
70 scATAC-seq simultaneously on the same cell) onto scATAC-seq references overcome the
71 shortcomings of shallow sequencing in co-assay data and improve the performance of clustering
72 and differentially accessible peaks calling. We integrated three datasets together (**Fig. 2a**), one
73 co-assay dataset of mouse adult cerebral cortex[6] (SNARE-seq), two scATAC-seq datasets of mouse
74 adult whole brain[5, 11] (sci-ATAC-seq and dscATAC-seq) that served as references, whose
75 sequencing depth are ~5 times deeper than the co-assay data. Single cells from three datasets
76 were mixed together without obvious batch effects by epiConv batch correction (**Fig. 2b**), while
77 other methods fail to do so (**Fig. S3a**). To assess whether the biological heterogeneity was
78 retained after batch correction, we performed conventional clustering on co-assay dataset (**Fig.
79 2a**) and joint clustering on integrated dataset (**Fig. 2d**, clusters were manually annotated by
80 canonical makers). More than 90% cells from each conventional cluster were assigned to only
81 one joint cluster by epiConv and rare cell types (e.g. C03/Ex 6 and C11/Ex 7, see number of co-
82 assay cells in **Fig. 2d**) were also clearly segregated. On the contrary, other methods were less
83 sensitive to rare cell types recognized by RNA-seq (**Fig. S3b**). We quantitatively evaluated the
84 consistency of clustering by Adjusted Mutual Information (AMI), where higher AMI suggested

higher consistency between conventional clustering and joint clustering after batch correction. EpiConv showed the most consistent results among all methods (0.81 in **Fig. 2d**; vs 0.66 and 0.63 in **Fig. S3b**). We also found that conventional cluster C09 could be further grouped into 3 cell types by joint clustering (**Fig. 2c**, clusters highlighted by red circles), which referred to one major cell type (oligodendrocyte) and two rare cell types (oligodendrocyte progenitor cell and microglia) based on their expression profiles from co-assay data (**Fig. 2d**), suggesting that joint analysis also revealed hidden rare cell types. Next, we examined whether single cells of co-assay data were correctly assigned to the reference. In each dataset, we performed differential analysis to get a set of marker peaks for each joint cluster to see whether these markers were conserved across different datasets. Although markers detected from two scATAC-seq references were consistent with each other, the results of co-assay data did not agree with them (**Fig. S4a**). Only markers of big clusters were conserved across three datasets (e.g. Ex 1-4). Moreover, a large number of cluster-specific markers could only be detected from deep sequencing references. We argued that this might be due to shallow sequencing of co-assay data and further incorporate RNA-seq profiles into our evaluation. To do that, we linked each peak to its closest gene promoter in the genome. Then for each cluster, we got a series of associated peaks with its cluster-specific marker genes (**Fig. 2e**). To quantitatively measure the consistency between ATAC-seq and RNA-seq profiles, we calculated the fold change of enrichment for two types of markers (N_{common} / (N_{ATAC} * N_{RNA}) * N_{total}; N_{common}: number of shared peaks, N_{ATAC}, number of chromatin markers, N_{RNA}, number of marker genes associated peaks, N_{total}, number of total peaks). We expected that peaks residing near the promoter of one gene were more likely to be its regulators and cluster-specific chromatin markers would enrich in the nearby regions of marker genes if joint analysis

correctly clustered recurrent cell types from co-assay and scATAC-seq datasets together. Indeed, we observed the enrichment and for most clusters, much more chromatin markers could be detected from scATAC-seq references than co-assay data and they were with similar or even higher extent of enrichment with marker gene associated peaks (**Fig. S4b**), proving that epiConv correctly assigned co-assay single cells to the references. We noted that there were few chromatin markers of Ex 6 and Ex 7 due to their small cluster size. In order to overcome this problem, we performed the analyses on 7 excitatory neuron clusters only and the results also supported the correctness of epiConv (**Fig. S4c,d**).

We also applied epiConv to another co-assay data of developmental mouse cortex to see whether epiConv performed well on continuous differentiation process. Specifically, we aligned co-assay data of postnatal day 0 mouse cerebral cortex[6] (SNARE-seq) to scATAC-seq data of E18 cortex, sequenced by 10x Genomics (**Fig. S5a**). By clustering and differential analyses used above, we demonstrated that epiConv correctly assigned co-assay cells to the reference (**Fig. S5b,c**). As the sequencing depth of co-assay data is deeper, we could directly validate the results of epiConv by shared chromatin markers of two datasets. And as expected, we could detect ~5 times more differentially accessible peaks from scATAC-seq reference than co-assay data (**Fig. S5c**). Moreover, we found 2,719 differentially accessible peaks detected from the reference showed consistent pattern with the expressions of their nearest genes along the differentiation path that was examined in original article[6] (from *Hmgn2*^{high} intermediate progenitors to *Cux1*^{high} excitatory neurons, J01 to J04). Results based on both distinct cluster and continuous pseudotime assessments proved that epiConv was able to group cells of the same developmental stages together from two independent datasets (**Fig. S5d,e**).

129 In addition to perform batch correction, integration algorithms could also be used to align
130 cells with different biological conditions or treatments together to identify shared cell
131 populations or perform reference-guided analyses. Here, we further benchmarked the
132 performance of epiConv by aligning malignant cells from mixed-phenotype acute leukemia
133 (MPAL), which was known to present with features of multiple hematopoietic lineages, to normal
134 hematopoiesis[12]. The normal hematopoiesis reference contains bone marrow mononuclear cells
135 (BMMCs) and CD34+ enriched BMMCs and the Leukemia data contains single cells from MPAL
136 patients[12]. After epiConv integration, all malignant cells were projected into several clusters of
137 normal cells (**Fig. 3a,b**). We first annotated clusters by comparing chromatin markers of normal
138 cells with the ATAC-seq profiles of FACS-sorted bulk samples[13] (**Fig. 3c**; **Fig. S6a**). In addition to
139 previously known cell types, we also found two novel clusters (C08 and C09). The C08 cluster (T
140 biased progenitor) was similar to stem cell cluster (C01) but was more accessible in the marker
141 regions of T cells (~ 50% up-regulated peaks in C08 against C01 are T cell markers) and the C09
142 cluster (unknown progenitor) was moderately accessible in myeloid, lymphoid and erythroid
143 lineage-specific regions. All malignant samples contained a large proportion of stem-like cells
144 (C01) but the composition of more differentiated cells varied among patients (**Fig. S6b**). The
145 enrichment pattern of cluster-specific markers under normal and malignant hematopoiesis
146 suggested that both abundant and rare leukemic cell types were assigned to the most similar
147 normal cells (**Fig. S6b**). In contrast, malignant and normal cells were still clustered by their
148 biological conditions and patients in the results of cisTopic and LSI (**Fig. S7a,b**). In the original
149 article, Granja *et al.*[12] developed a novel approach to project leukemic cells to normal
150 hematopoiesis. We found that although it still failed to integrate malignant with normal cells

151 through joint clustering and embedding (**Fig. S7c**), which suggested that the variations between
152 leukemic and normal cells were not corrected, it performed better by projecting malignant cells
153 to an existing embedding of normal cells (add new unseen data points to existing embedding by
154 UMAP), just slightly worse than epiConv (**Fig. 3d,e**). Given malignant cells always contained mixed
155 epigenetic programs of several normal cell types, it was hard to benchmark the results by
156 canonical markers. Instead, we calculated the total number of differentially accessible peaks
157 detected by hypergeometric test under malignant hematopoiesis (higher cluster purity results in
158 more differentially accessible peaks to be detected, which is confirmed by permutation on real
159 data), and the number of recalled markers (markers of one cluster that can be detected from
160 both normal and malignant cells), which reflected consistency of hierarchy between normal and
161 malignant cells. EpiConv showed better performance than Granja *et al.*'s method by detecting
162 more differentially accessible peaks and recalled peaks (**Fig. 3f**). Moreover, malignant cells were
163 not always assigned to the most similar normal cells by Granja *et al.*'s method when comparing
164 the overlap of cluster-specific markers under normal and malignant hematopoiesis (e.g.
165 malignant cells assigned to GMPs by Granja *et al.*'s method were actually more similar to
166 monocytes). Through comparison of cluster-specific markers under normal and malignant
167 hematopoiesis by epiConv, it could be seen that recalled peaks only explained a small fraction of
168 heterogeneity of malignant cells, implying that leukemic cells might have alternative routes to
169 form hierarchy. Moreover, the alternative hierarchy of malignant cells might be easily missed by
170 other methods given that they could not deconvolute highly similar malignant cells into multiple
171 cell types (**Fig. S7**). Motivated by this thinking, we classified cluster-specific markers into three
172 types (**Fig. S8**): 1) hierarchy conserved (shared by normal and malignant hematopoiesis); 2)

173 hierarchy loss (unique to normal hematopoiesis); 3) hierarchy gain (unique to malignant
174 hematopoiesis). The conserved hierarchies were controlled by the transcription factors that were
175 known to be important for hematopoiesis (e.g. RUNX in HSCs and MPPs, PU.1 in myeloid
176 lineages, E2A in lymphoid lineages, GATA in erythroid lineages). While the hierarchies unique to
177 normal hematopoiesis were controlled by the coordination of several epigenetic modifiers, they
178 were largely lost in malignant hematopoiesis (e.g CTCF lost in stem cells and erythroid lineages,
179 C/EBP in myeloid lineages). These results highlighted the power of epiConv to learn the
180 heterogeneity of malignant cells through reference-guided analyses.
181 In this paper, we demonstrate the epiConv performed well in joint analysis of scATAC-seq data
182 under various situations. Moreover, joint analysis provided deeper insights into the epigenetic
183 regulation of single cells of different developmental stages as well as disease conditions. EpiConv
184 is also computationally efficient and can be scaled to datasets with tens of thousands of cells
185 (**Table S1**). We believe that the computational framework in this study along with technical
186 improvements could facilitate better interpretation of the roles of chromatin accessibility in gene
187 regulation in the future.
188

189 Methods

190 **Calculate the similarity matrix by epiConv** EpiConv first calculated the similarity matrix *S*
191 between single cells from a binarized matrix *M*, where rows represent peaks and columns
192 represent cells. The similarity between two cells is calculated by the dot product of two cell
193 vectors, which means that the similarity matrix is calculated by $M^T M$. After normalization by
194 library size, the similarity matrix can be used for other downstream analyses. A detailed

195 description of this step can be found in Supplementary Note 1.

196

197 **Correct batch effects by epiConv** If single cells are from more than one batch, further steps are

198 required to remove the batch effects (**Fig. 1b**). We first apply Eigenvalue Decomposition to

199 normalized similarity matrix *S* and keep *r* Eigen values with largest absolute values and their

200 corresponding Eigen vectors *X*. The similarity matrix *S* can be approximated by matrix product of

201 matrix *X*, which contains Eigen vectors and diagonal matrix *Λ*, whose diagonal elements contains

202 Eigen values. The difference between *S* and its approximation is stored in residual matrix $S_{residual}$.

203 Eigen vectors *X* captures batch derived variations and we assume that batch effects can be

204 corrected by properly scaling *X* (**Fig. S9a,b**).

205 Next, we need to learn the recurrent cell populations across datasets. For simplicity, assume that

206 we have one reference dataset *A* and one target dataset *B* that needs be aligned to the reference

207 (**Fig. S9c**). For each cell in *B*, we find its k_1 nearest neighbors in *A* based on the similarity matrix.

208 For each cell in *A*, we find its k_2 nearest neighbors in *B*. If one cell in *B* (cell *b*) find a true neighbor

209 in *A* (cell *a*) among its k_1 neighbors, we expect that cell *b* should be similar with cell *a*'s k_2

210 neighbors in *B*. To quantitatively measure the similarity between *b* and *a*'s k_2 neighbors, we

211 require a collection of features of *B* as guiding features (we will discuss later how to obtain these

212 features). For each guiding feature, we calculate the mean and standard deviation of cell *a*'s k_2

213 neighbors and Z-score normalize the feature value of cell *b* accordingly. If cell *b* shows strong

214 deviation from cell *a*'s k_2 neighbors ($|Z\ score| > threshold_Z$) for any guiding feature, we think

215 cell *a* is a false neighbor of cell *b* and break the link. After such filtering, some cells in *B* may still

216 keep several neighbors in *A* among its initial k_1 neighbors (true neighbors) while others may lose

most of its initial k_1 neighbors. Cells in *B* that have enough true neighbors in *A* (> 5 in this study) are used as anchors for batch correction. For each anchor in *B*, we calculated the difference of Eigen vectors between itself and its true neighbors in *A* as the scaling parameters. The scaling parameters for other non-anchor cells are calculated by the weighted mean of its nearest anchors (10 anchors in this study) on a shared nearest neighbors graph (SNN graph) of *B*, where the weight is equal to the edge of SNN graph. Finally, the corrected eigenvectors $X_{corrected}$ is calculated by scaling *X* accordingly (**Fig. S9b**).

Parameters settings depend on the complexity and size of data. First, the number of Eigen vectors (*r*) depends on the complexity of data and an appropriate *r* can be easily obtained by manually examining the batch effects on Eigen vectors like **Fig. S9a**. The number of neighbors (k_1 and k_2) and $threshold_Z$ control the number of anchors obtained. Smaller k_1 and $threshold_Z$ means more stringent filtering and fewer anchors. However, we expected that the number of anchors should be at least ~20% of total cells for each dataset and distributed in all clusters (**Fig. S9d**). As we do not filter cells in k_2 neighbors, k_2 should be set to a smaller value compared to k_1 to prevent from picking too much false neighbors. In this study, we use $r = 30, k_1 = 50, k_2 = 10$ unless otherwise noted.

Here, we discuss how to obtain the guiding features and SNN graph of dataset *B*. If dataset *B* is scATAC-seq data, the Eigen vectors calculated above can be just used as guiding features given that Eigenvalue Decomposition also captures major biological variations. The SNN graph can be calculated based on the similarity matrix *S* with K-nearest neighbor set to 1% of total cells in *B* (no smaller than 20 or larger than 200). If dataset *B* is co-assay data, we use the Eigen vectors and first 50 principal components (PCs) of gene expressions from RNA-seq as guiding features. The

239 SNN graph is calculated based on the information from RNA-seq or together with ATAC-seq,
240 depending on the data quality of RNA-seq and ATAC-seq (see below for each co-assay dataset).
241 Notably, the guiding features and SNN graph calculated by other methods are also compatible
242 with epiConv if they better resolve the intra-population structure of the dataset.
243 EpiConv supports of multiple reference datasets and multiple target datasets. When multiple
244 references and target datasets are available, we first integrate all references together (scale Ref *B*
245 to match Ref *A* by finding Ref *B*'s neighbors in Ref *A*, then scale Ref *C* to match Ref *A* and Ref *B* by
246 finding Ref *C*'s neighbors in Ref *A* and Ref *B* …) and then align each target dataset to the
247 references by finding their neighbors in all references.
248 After the Eigen vectors of all datasets are properly scaled, the corrected similarity matrix is
249 calculated from $X_{corrected}$, the diagonal matrix Λ and the residual matrix $S_{residual}$ (**Fig. 1b**).
250
251 **Dimension reduction and clustering of epiConv** Given the similarity matrix *S*, we used Uniform
252 Manifold Approximation and Projection[14] (UMAP) in R package UMAP for dimension reduction
253 and Louvain algorithm implemented in R package Seurat[15] for clustering. In order to reduce
254 noise, the similarity matrix between cells is first transformed to SNN graph (S_{snn}) described above.
255 Then, the distance matrix (Max (S_{snn}) - S_{snn}) is used as UMAP input. The Louvain clustering is
256 performed on the transformed UMAP graph *G* from the distance matrix (Max (S_{snn}) - S_{snn}) to
257 generate consistent results between dimension reduction and clustering. All unmentioned
258 settings are set to default values and the resolution setting in Louvain clustering is manually
259 adjusted between 0.2 and 0.8.
260

261 **Detect differentially accessible peaks** We use hypergeometric test to detect cluster-specific
262 accessible peaks. Population size was defined as total number of cells. Sample size was defined as
263 the total library size of cluster divided by the mean library size of all cells. No. of success in the
264 population for each peak was defined as total number of cells with coverage. No. of success in
265 the sample was defined as number of cells with coverage in this cluster. Only peaks that were
266 accessible in at least 1% cells were tested. Peaks with one-tailed p-value smaller than 0.01 were
267 considered as differentially accessible peaks. If peaks were considered as differentially accessible
268 peak in more than one cluster based on the statistical significance threshold, we assigned the
269 peak to the cluster with lowest p-values.
270
271 **Peak calling and matrix counting** We used peaks defined by original article or called peaks from
272 ends of fragments by MACS2[16] (--nomodel --nolambda --keep-dup all --shift -95 --extsize 200) if
273 processed peak file was unavailable. We counted the ends of fragments against peaks to obtain
274 the count matrix. The count matrix was binarized first for further analyses.
275
276 **Application of other methods** We applied cisTopic[9] and Latent Sematic Indexing[4] (LSI) to scATAC-
277 seq data and used Harmony[10] to remove batch effects. In cisTopic, the number of topics was set
278 to 20, 30, 40 and 50 and automatically determined. In LSI, we filtered peaks that were accessible
279 in less than 1% cells. The number of reduced dimensions was set to 50. We applied Harmony on
280 the topics learned by cisTopic or PCs learned by LSI without further PCA transformation. Other
281 unmentioned settings were all set to defaults. We performed Louvain clustering on Harmony
282 corrected topics or PCs by Seurat. In order to benchmark batch correction, entropy of batch

283 mixing was calculated by the information entropy of batch among each cell's 200 nearest
284 neighbors after batch correction, where higher information entropy meant better mixing of cells
285 from different batches.
286
287 **Comparison of EpiConv with other methods in individual dataset (without batch effect).** The
288 5,000 PBMCs data was processed as described above. In order to assess the performance of
289 epiConv and other methods on cell lines data[3], we clustered cells into 8 clusters (the true number
290 of cell types) by louvain clustering and used Adjust Rand Index (ARI) to evaluate the accuracy.
291
292 **scATAC-seq data of PBMCs** We applied epiConv and other methods on two published PBMC
293 datasets. The dataset contains 7 batches of cells. The data from GSE129785 contains two batches
294 of PBMCs, two batches of CD4+CD45RA+ naïve T cells and two batches of CD4+CD45RA- memory
295 T cells[8]. The data from GSE123581 contains isolated CD4+ T cells, CD8+ T cells, CD19+ B cells,
296 CD14+ monocytes and CD56+ NK cells and was treated as one batch[5]. Two replicates of PBMCs of
297 GSE129785 were used as references in epiConv. The threshold$_Z$ was set to 1.5 in this dataset as
298 we found that CD4+ T cells and CD8+ T cells were easily mixed and applied a more stringent
299 threshold. Differential analyses were performed on cells with known cell types. Given T cells
300 shared many common features, we performed differential analyses on CD4+ naïve vs. CD4+
301 memory T cells of GSE129785 and CD8+ naïve, CD8+ effector and CD4+ T cells of GSE123581 to
302 learn their marker regions instead of comparing them with all other cells.
303
304 **scATAC-seq data of adult mouse brain** We integrated co-assay data of mouse adult cerebral

305 cortex from GSE126074[6] (SNARE-seq), scATAC-seq of mouse adult whole brain from Mouse Cell
306 Atlas[11] (sci-ATAC-seq) and GSE123581[5] (dscATAC-seq) together. For RNA-seq of co-assay data, we
307 used a common pipeline of Seurat with default settings (find 2,000 most variable genes and
308 obtain 50 PCs from them) to perform dimension reduction, clustering and finding cluster-specific
309 marker genes. Given that the sequencing depth of RNA-seq is deep but that of ATAC-seq is
310 shallow, we calculated the SNN graph from the first 50 PCs of RNA-seq data only. For ATAC-seq
311 analyses, we first aligned dscATAC-seq data to sciATAC-seq data and then aligned co-assay data to
312 them. The number of Eigen vectors (r) was set to 40 and k_1 was set to 100 as the reference
313 datasets were large. Dimension reduction and joint clustering were performed on integrated
314 dataset as described above. Performances of clustering by different methods were evaluated by
315 Adjusted Mutual Index (AMI). Given that the resolution of Louvain clustering affected AMI, we
316 performed clustering with resolution from 0.2 to 2.0 for cisTopic and LSI and the highest AMI
317 were reported. For epiConv, we reported the AMI of joint clustering in **Fig. 2d**. The cluster-specific
318 markers shared by sci-ATAC-seq and dscATAC-seq were shown and used for infer the relationships
319 between ATAC-seq and RNA-seq. We also performed differential analysis on excitatory neuron
320 cells instead of all cells to better detect the cluster-specific markers of rare cell types (Ex 6 and Ex
321 7).
322
323 **scATAC-seq data of developmental mouse brain** we aligned the SNARE-seq of postnatal day 0
324 mouse cerebral cortex[6] to scATAC-seq data of E18 cortex, sequenced by 10x Genomics. As the
325 sequencing depth of RNA-seq is shallow and we cannot clearly resolve the relationships of single
326 cells based on RNA-seq only, we combined the first 50 PCs of RNA-seq and first 50 Eigen vectors

327 of ATAC-seq to perform low dimensional embedding and clustering using the pipeline of Seurat.
328 The SNN graph used in batch correction was calculated on 100 combined features from RNA-seq
329 and ATAC-seq. Clustering and differential analysis were performed as described above. Clusters of
330 astrocytes (J12) and *Hmgn*^{high} Intermediate progenitors (J01) were similar with each other and
331 formed one cluster in unsupervised clustering. We performed further clustering to segregate
332 them. Clusters J14, J15 and J16 were excluded in differential analysis as they did not contain co-
333 assay cells or were mixtures of rare cell types due to lack of proper reference cells. Cell types
334 were labeled based on canonical markers. To investigate the changes of chromatin states and
335 gene expression along differentiation, we also perform differential analyses on ATAC-seq and
336 RNA-seq on 4 clusters (J01 to J04) and selected consistent chromatin markers and gene markers
337 (up-regulated in the same cluster). For cells sequenced by 10x Genomics from J01 to J04, we
338 constructed their pseudotime axis by the sum of the number of accessible peaks among J04
339 markers minus that of J01 followed by library size normalization as we observed that from J01 to
340 J04, most J01 markers gradually lost accessibility while J04 markers gained accessibility. Next, we
341 imputed the ATAC-seq counts from their 20 nearest neighbors from 10x Genomics data and
342 imputed the RNA-seq counts from their 20 nearest neighbors from SNARE-seq data. Finally, the
343 ATAC-seq counts and RNA-seq counts were normalized by library size with RNA-seq counts
344 further log2 transformed, and they were smoothed along the pseudotime axis by smooth.spline()
345 function in R.
346
347 **scATAC-seq data of Leukemia** EpiConv integration, dimension reduction, clustering and
348 differential analysis were performed as described above. There were other two samples (MPAL2

349 and MPAL5 relapse) in Granja *et al.* 2019[12]. Although we could align them to normal
350 hematopoiesis, they share few common markers with normal cells compared to other samples.
351 We thought it was inappropriate to compare them with normal hematopoiesis and did not show
352 the results of these two samples. To test Granja *et al.*'s method, we first performed LSI on normal
353 cells with 25,000 differentially accessible peaks of lowest *p*-values, kept first 25 PCs, and
354 calculated the PCs of malignant cells using the parameters inferred normal cells. Then we applied
355 UMAP to the PCs of normal and malignant cells (joint embedding) or first applied UMAP to the
356 PCs of normal cells and then calculated the embedding of malignant cells by adding new unseen
357 data points (malignant cells) into existing embedding (projection to existing embedding). We
358 used the clusters from epiConv to annotate normal cells and the labels of malignant cells were
359 assigned based on its nearest normal cell in the embedding of UMAP.
360 Motif calling was performed by Homer[17] on the ± 200 bp regions from peak centers. The length
361 of motif was set to 8, 10 and 12. All ATAC-seq peaks were used as background. Motifs that were
362 in fewer than 10% examined peaks were not shown. In T and NK cell lineages, we always called
363 several motifs with low information content and higher GC content. These motifs did not show
364 high consistency with known motifs and were not shown.
365
366 **Data availability** All data analyzed in this article are available in public databases and are
367 summarized in **Table S1**. EpiConv is available in Github (https://github.com/LiLin-
368 biosoft/epiConv).
369
370

References:

1. Buenrostro, J.D., Giresi, P.G., Zaba, L.C., Chang, H.Y. & Greenleaf, W.J. Transposition of native chromatin for fast and sensitive epigenomic profiling of open chromatin, DNA-binding proteins and nucleosome position. *Nat Methods* **10**, 1213-1218 (2013).
2. Klemm, S.L., Shipony, Z. & Greenleaf, W.J. Chromatin accessibility and the regulatory epigenome. *Nat Rev Genet* **20**, 207-220 (2019).
3. Buenrostro, J.D. et al. Single-cell chromatin accessibility reveals principles of regulatory variation. *Nature* **523**, 486-490 (2015).
4. Cusanovich, D.A. et al. Multiplex single cell profiling of chromatin accessibility by combinatorial cellular indexing. *Science* **348**, 910-914 (2015).
5. Lareau, C.A. et al. Droplet-based combinatorial indexing for massive-scale single-cell chromatin accessibility. *Nat Biotechnol* **37**, 916-924 (2019).
6. Chen, S., Lake, B.B. & Zhang, K. High-throughput sequencing of the transcriptome and chromatin accessibility in the same cell. *Nat Biotechnol* **37**, 1452-1457 (2019).
7. Orchard, P., Kyono, Y., Hensley, J., Kitzman, J.O. & Parker, S.C.J. Quantification, Dynamic Visualization, and Validation of Bias in ATAC-Seq Data with ataqv. *Cell Syst* **10**, 298-306 e294 (2020).
8. Satpathy, A.T. et al. Massively parallel single-cell chromatin landscapes of human immune cell development and intratumoral T cell exhaustion. *Nat Biotechnol* **37**, 925-936 (2019).
9. Bravo Gonzalez-Blas, C. et al. cisTopic: cis-regulatory topic modeling on single-cell ATAC-seq data. *Nat Methods* **16**, 397-400 (2019).
10. Korsunsky, I. et al. Fast, sensitive and accurate integration of single-cell data with Harmony. *Nat Methods* **16**, 1289-1296 (2019).
11. Cusanovich, D.A. et al. A Single-Cell Atlas of In Vivo Mammalian Chromatin Accessibility. *Cell* **174**, 1309-1324 e1318 (2018).
12. Granja, J.M. et al. Single-cell multiomic analysis identifies regulatory programs in mixed-phenotype acute leukemia. *Nat Biotechnol* **37**, 1458-1465 (2019).
13. Corces, M.R. et al. Lineage-specific and single-cell chromatin accessibility charts human hematopoiesis and leukemia evolution. *Nat Genet* **48**, 1193-1203 (2016).
14. McInnes, L., Healy, J. & Melville, J. UMAP: Uniform Manifold Approximation and Projection for Dimension Reduction. *arXiv* https://arxiv.org/abs/1802.03426v3 (2020).
15. Stuart, T. et al. Comprehensive Integration of Single-Cell Data. *Cell* **177**, 1888-1902 e1821 (2019).
16. Zhang, Y. et al. Model-based analysis of ChIP-Seq (MACS). *Genome Biol* **9**, R137 (2008).
17. Heinz, S. et al. Simple combinations of lineage-determining transcription factors prime cis-regulatory elements required for macrophage and B cell identities. *Mol Cell* **38**, 576-589 (2010).

Acknowledgements

This project was funded by the National Key Research and Development Program of China (2018YFC1004602), National Natural Science Foundation of China (NSF 31871332) and a startup fund to L.Z. from ShanghaiTech University. We would like to thank Vinay Kartha and Xiaoqi Zheng for useful suggestions. We would like to thank Xiaojing Zhao for testing the reproducibility of the study. We would like to thank Yingdong Zhang on his technical support on the HPC platform of ShanghaiTech University.

Author contributions

L.L. conceived the study, developed the methods and performed the analyses. L.L. and L.Z. wrote the manuscript. L.Z supervised the study.

Competing interests

The authors declare no competing interests.

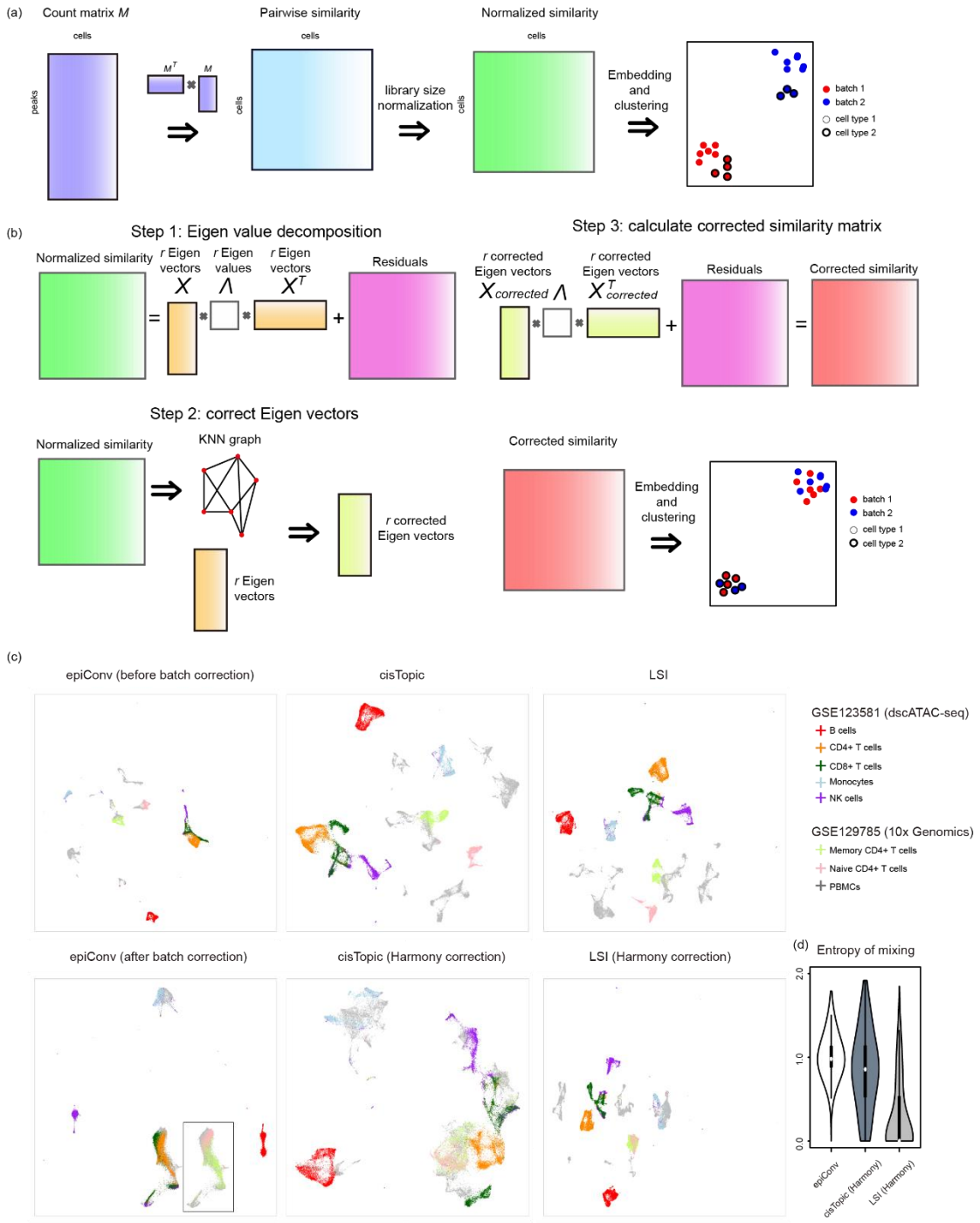

Figure 1 An overview of epiConv algorithm. (**a**) The workflow of calculating similarity matrix between single cells. (**b**) The workflow of batch correction. (**c**) epiConv better corrects batch effects than other methods on a collection of PBMCs datasets. (d) The entropy of batch mixing among cells' nearest neighbors after batch correction of Figure 1c.

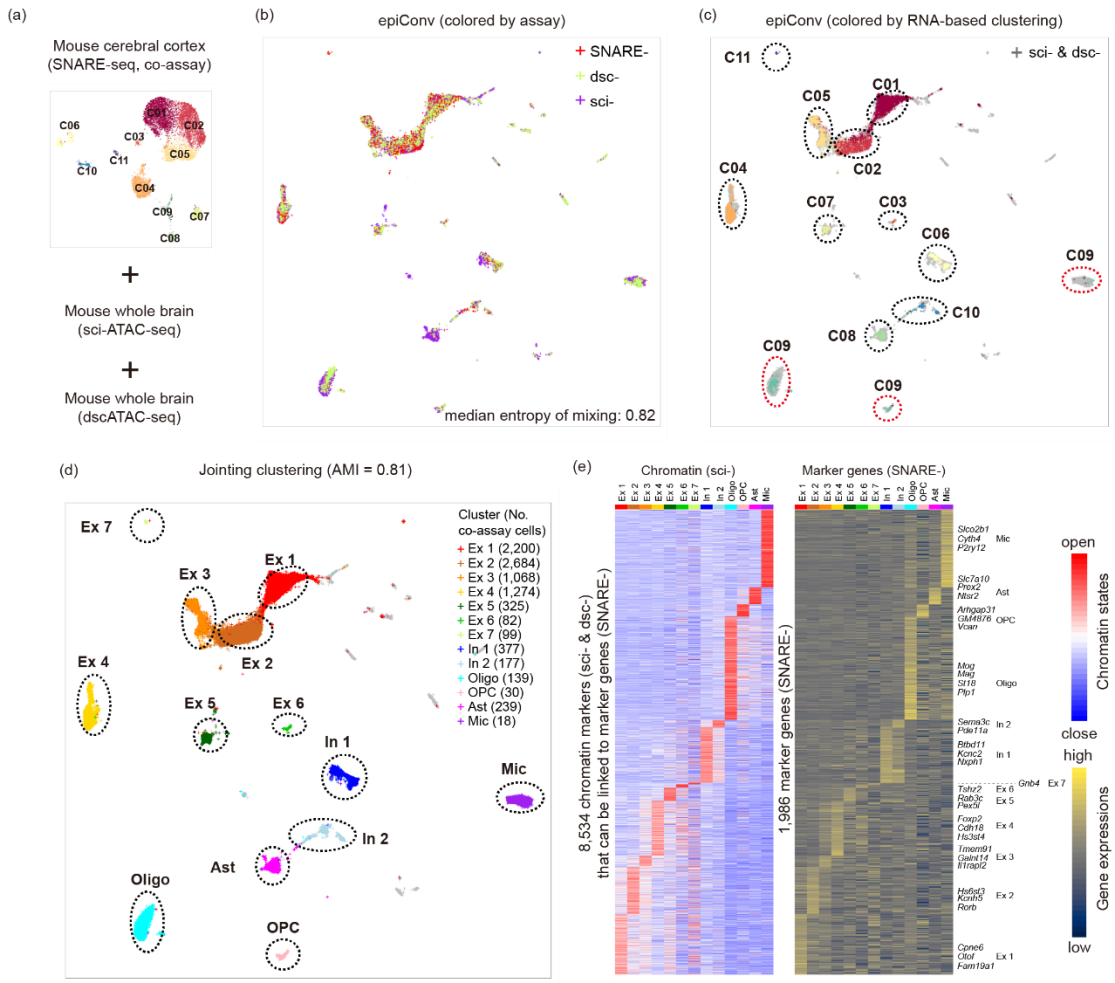

Figure 2 Aligning co-assay (SNARE-seq) data of mouse cerebral cortex to scATAC-seq (sci-ATAC-seq and dscATAC-seq) references increases the resolution of chromatin profiles. (**a**) Low dimensional embedding and clustering of co-assay data. (**b**) Joint embedding of co-assay data and scATAC-seq references, cells are colored by assays. Median value of entropy of batch mixing is shown in bottom right. (**c**) Joint embedding of co-assay data and scATAC-seq references, cells of co-assay data are colored according to conventional clustering in (**a**). Cells of scATAC-seq references are colored in grey. (**d**) Joint embedding of co-assay data and scATAC-seq references, cells are colored by manually annotated joint clusters. Ex, excitatory neuron; In, inhibitory neuron; Oligo, oligodendrocyte; OPC, oligodendrocyte progenitor cell; Ast, astrocyte; Mic, microglia. (**e**) Left: heatmap of chromatin markers detected from scATAC-seq references that can be linked to marker genes. Right: expressions of the corresponding marker genes detected from RNA-seq of co-assay data. Selected marker genes with highest fold changes are shown in the right panel.

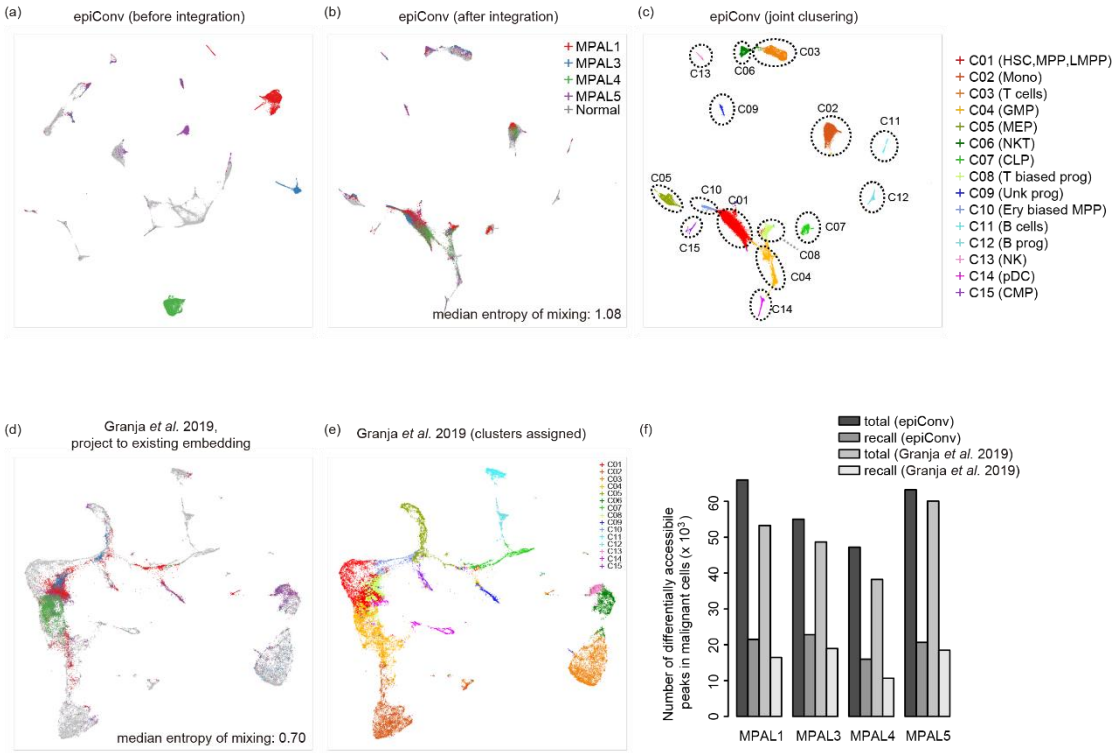

Figure 3 Aligning malignant cells to normal hematopoiesis reveals the hidden epigenetic hierarchy of leukemia. (**a**) Low dimensional embedding of epiConv before integration. (**b**) Low dimensional embedding of epiConv after integration. (**c**) Joint clustering of normal and malignant cells by epiConv. HSC, hematopoietic stem cell; MPP, multipotent progenitors; LMPP lymphoid-primed multipotent progenitor; Mono, monocyte; GMP, granulocyte-macrophage progenitor; MEP, megakaryocyte-erythroid progenitor; CLP, common lymphoid progenitor; Ery biased MPP, erythroid biased MPP; pDC, plasmacytoid dendritic cell; CMP, common myeloid progenitor. (**d**) Low dimensional embedding of Granja *et al.*'s method by projecting malignant cells to existing embedding of normal cells. Cells in (**a**), (**b**) and (**d**) are colored by patients. Median values of entropy of batch mixing in (**b**) and (**d**) are shown in bottom right. (**e**) Cluster assignments by Granja *et al.*'s method. Clusters of normal cells are identical as (**c**) and clusters of malignant cells are assigned based on their nearest normal cells. (**f**) Number of differentially accessible peaks in total and number of recalled differentially accessible peaks under normal and malignant hematopoiesis.

Supplementary Materials

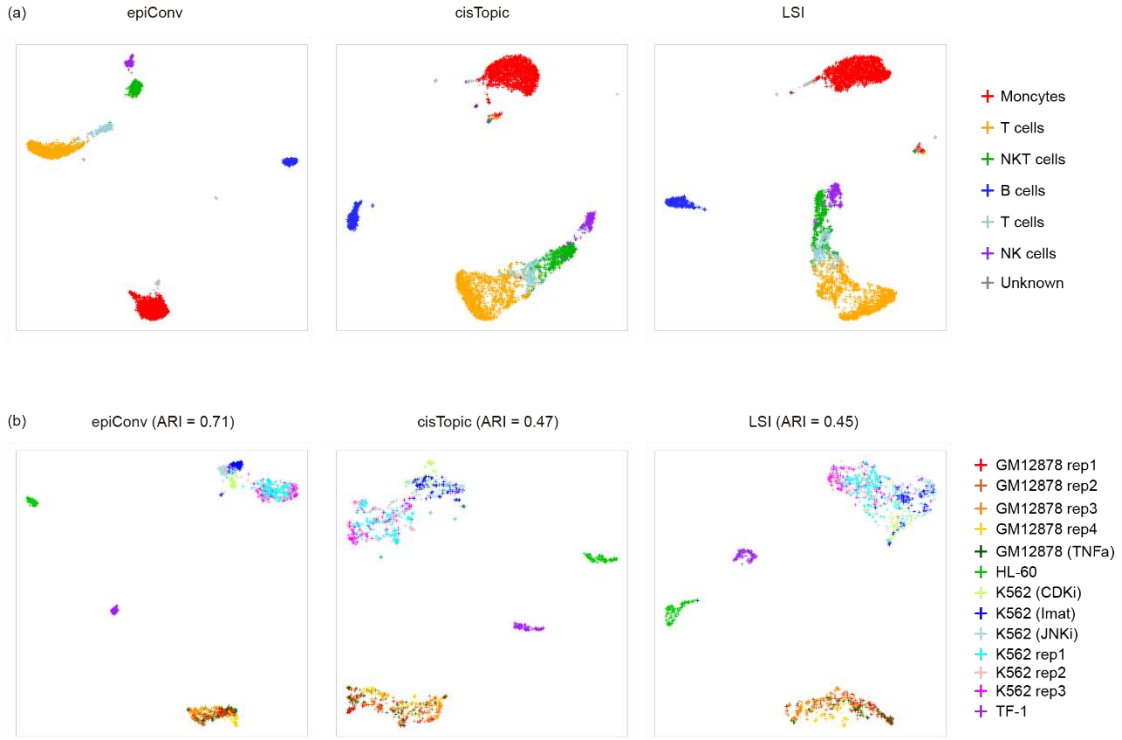

Figure S1 Comparison of epiConv with cisTopic and LSI. (**a**) Low-dimensional embedding of 5,000 PBMCs. Clusters are inferred from epiConv and manually annotated. Results from three methods are largely consistent. (**b**) Low-dimensional embedding of cell lines data. Cells are colored by their identities. Clustering of epiConv achieves higher Adjusted Rand Index (ARI) as it better segregates K562 cells treated by different drugs from untreated cells.

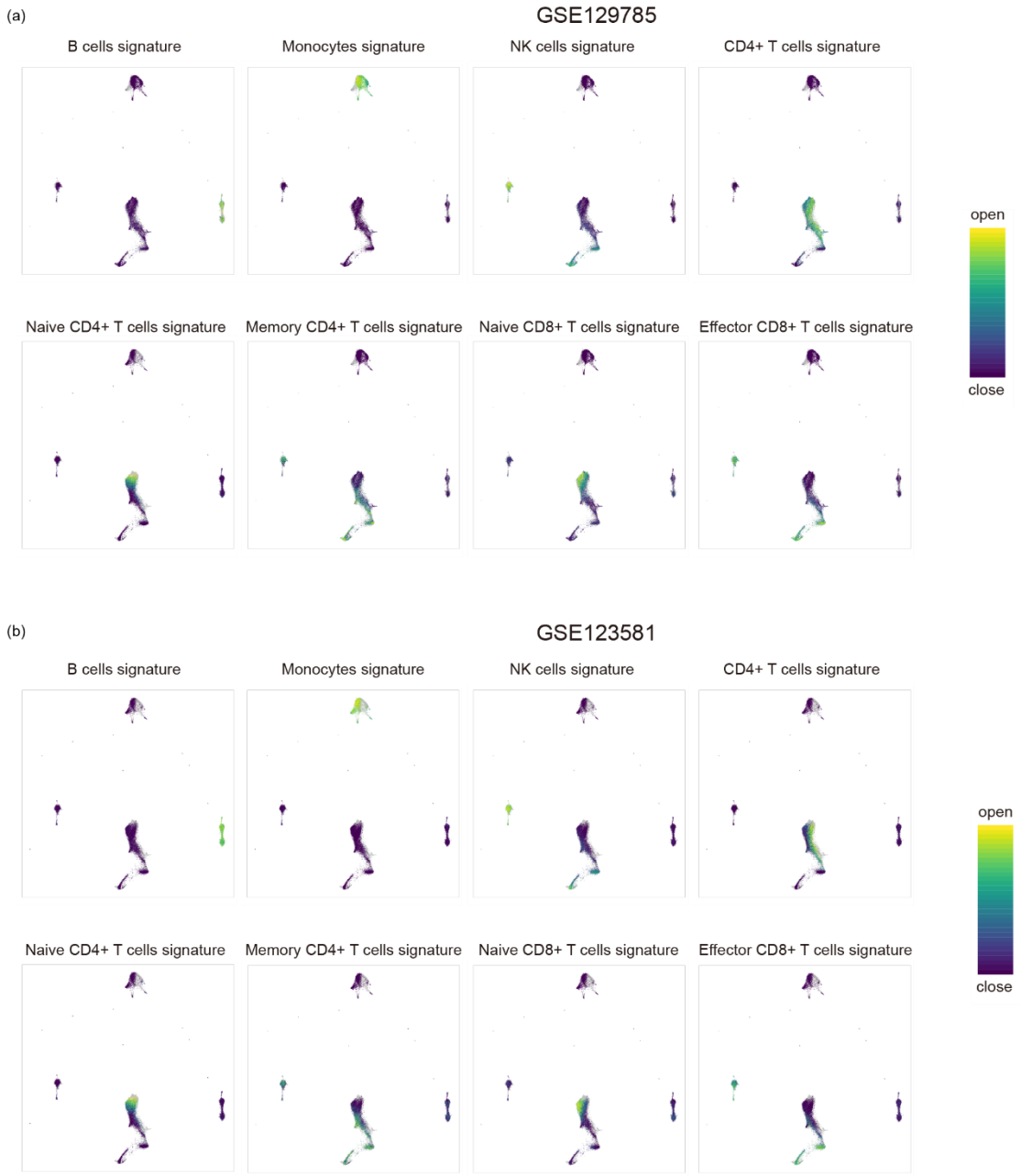

Figure S2 Supplementary figures for **Fig. 1c**. (**a**) Cell type specific signatures of PBMCs from GSE129785. (**b**) Cell type specific signatures of PBMCs from GSE123581.

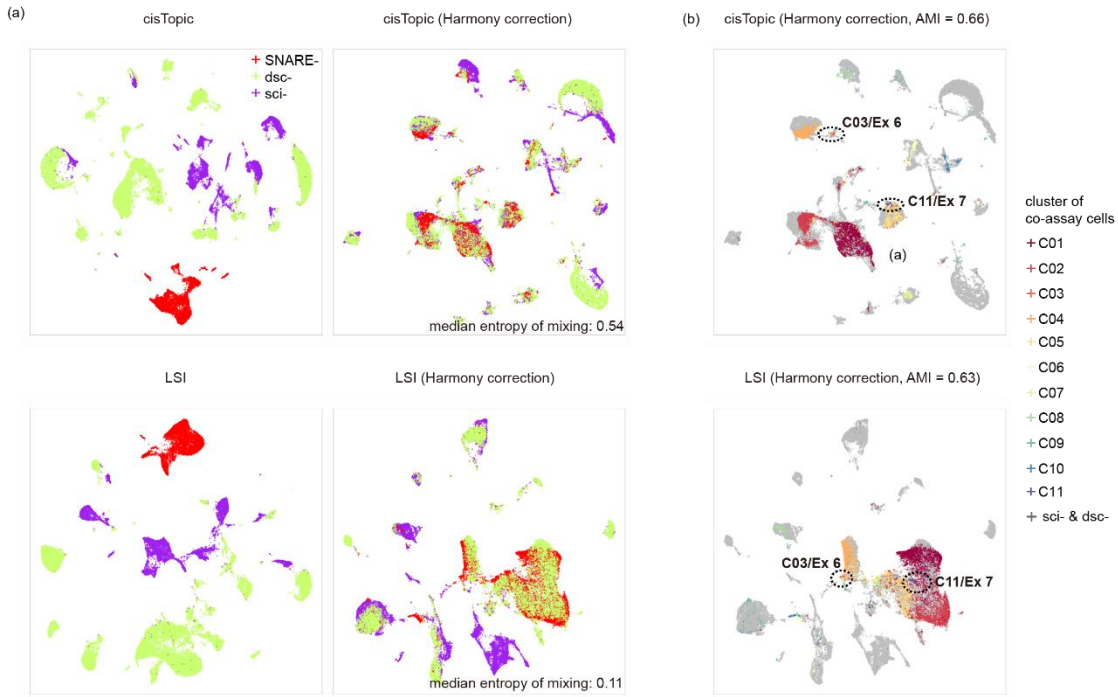

Figure S3 Benchmarking of cisTopic and LSI on adult mouse brain data. (**a**) Low-dimensional embedding of cisTopic and LSI before and after Harmony correction. Cells are colored by assays. Median values of entropy of batch mixing after batch correction are shown in bottom right. (**b**) Low-dimensional embedding of cisTopic and LSI after Harmony correction. Cells are colored according to conventional clustering of co-assay single cells in **Fig. 2a**. Cells of scATAC-seq references are colored in grey. Rare cell types of co-assay data (C03/Ex 6 and C11/Ex 7) are highlighted by dashed circles.

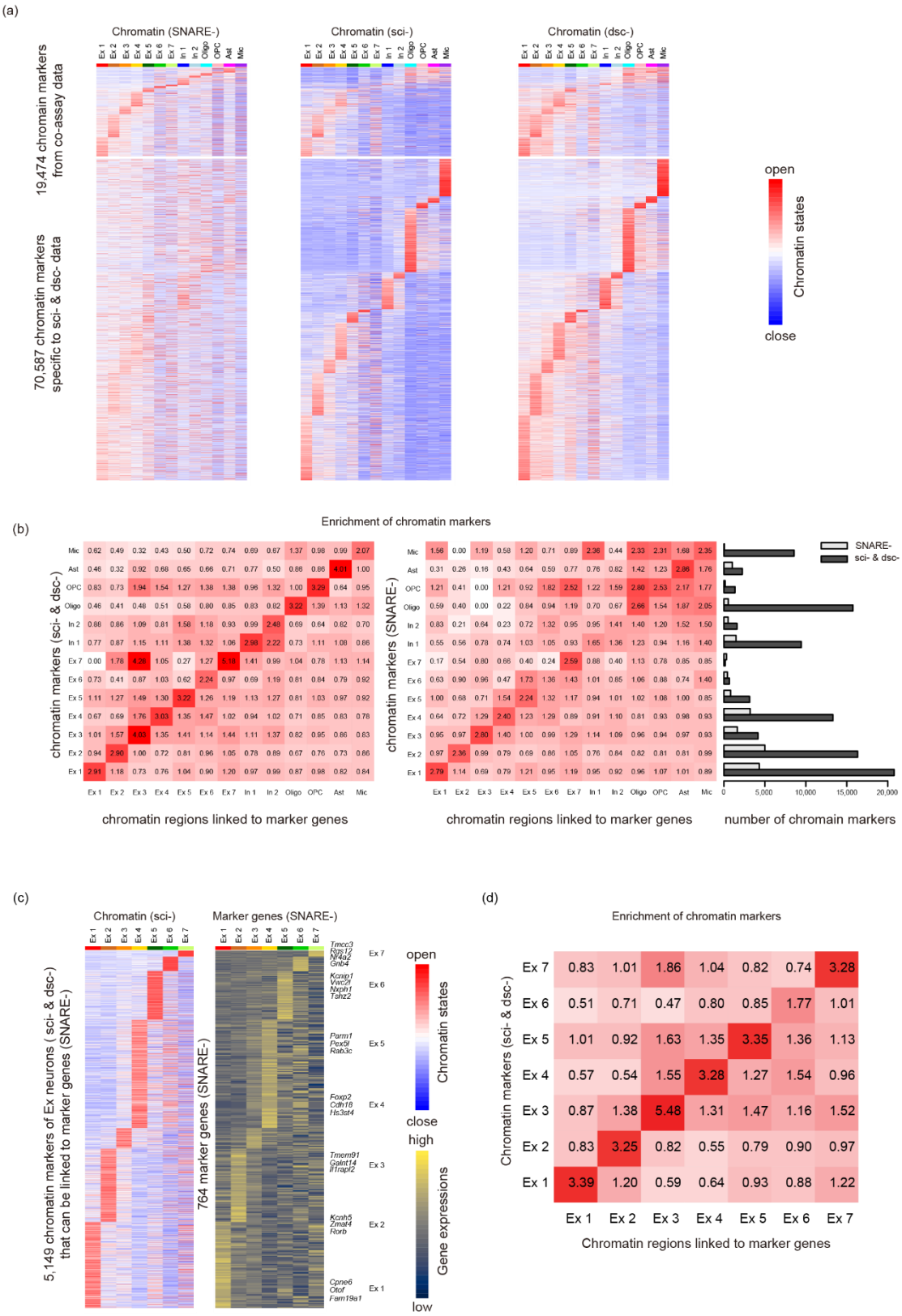

Figure S4 supplementary figures for **Fig. 2**. (**a**) Heatmaps of cluster-specific marker regions detected from ATAC-seq of co-assay data and two scATAC-seq references. Each column represents one aggregated ATAC-seq profiles of cells from corresponding joint clusters. (**b**) Left (scATAC-seq) and middle (co-assay): The fold changes of enrichment between ATAC-seq defined marker regions and RNA-seq defined associated regions. Right: the number of detected markers from scATAC-seq

references and co-assay data for each cluster. (**c**) Heatmaps of chromatin marker regions of excitatory neurons detected from scATAC-seq references (left) and the expressions of corresponding marker genes (right). Selected marker genes with highest fold changes are shown in the right panel. (**d**) The fold changes of enrichment between ATAC-seq defined marker regions and RNA-seq defined associated regions among excitatory neurons.

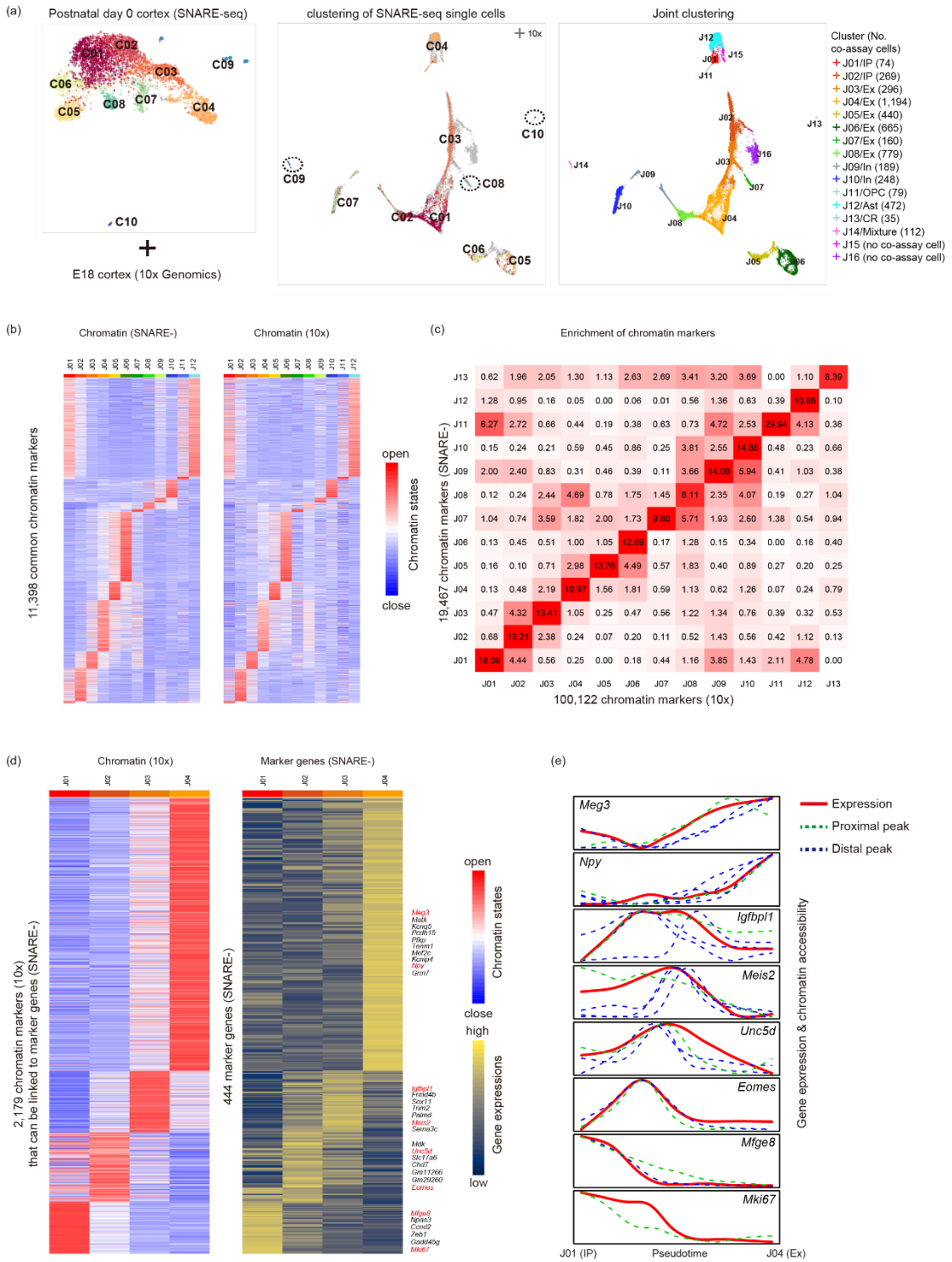

Figure S5 Aligning co-assay (SNARE-seq) data of postnatal day 0 mouse cortex to scATAC-seq (10x Genomics) reference. (**a**) Left: low dimensional embedding and conventional clustering of co-assay data. Middle: joint embedding of co-assay data and scATAC-seq reference, cells of co-assay data are colored according to conventional clustering in the left. Right: joint embedding of co-assay data and scATAC-seq data, cells are colored according to annotated joint clusters. IP, intermediate progenitor; CR, Cajal–retzius cell. (**b**) Heatmaps of cluster-specific chromatin markers shared by two datasets. Each column represents one aggregated ATAC-seq profiles of joint clusters. (**c**) The fold changes of enrichment between chromatin markers detected from

ATAC-seq of co-assay data and scATAC-seq reference. (**d**) Changes of chromatin states and gene expressions from intermediate progenitors to excitatory neurons (J01-J04). Left: heatmap of chromatin markers detected from scATAC-seq reference that can be linked to marker genes. Right: expressions of the corresponding marker genes. Selected marker genes with highest fold changes are shown in the right panel. (**e**) Smoothed chromatin and expression profiles of selected makers along the pseudotime of differentiation.

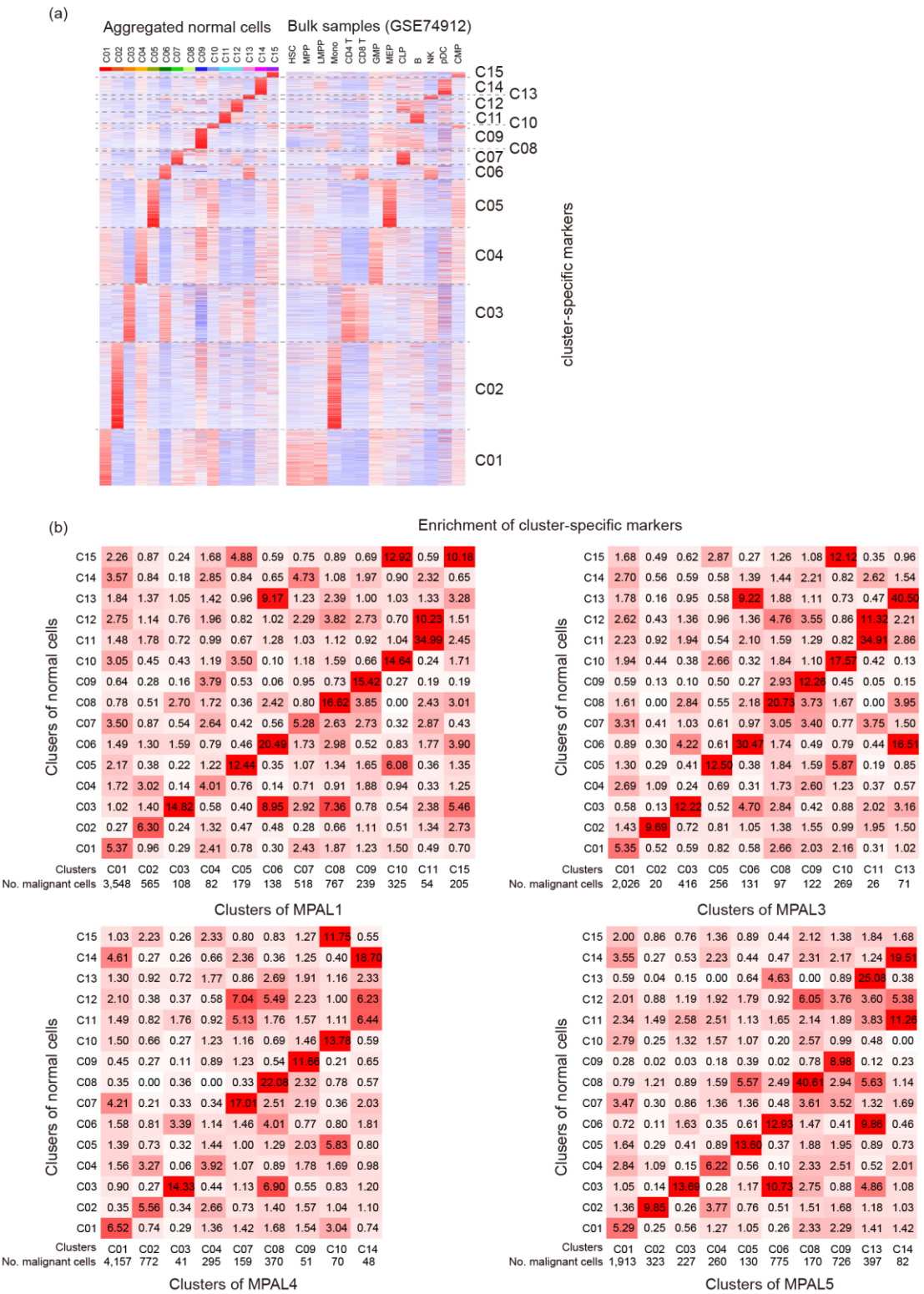

Figure S6 Supplementary figures for **Fig. 3.** (**a**) The aggregated ATAC-seq profiles of normal cells (left) and bulk samples (right) on chromatin marker regions, showing biological identities of each joint cluster. (**b**) The fold change of enrichment between markers detected from normal cells and malignant cells. Number of malignant cells in each cluster is shown on the bottom. Clusters with fewer than 20 cells are not shown.

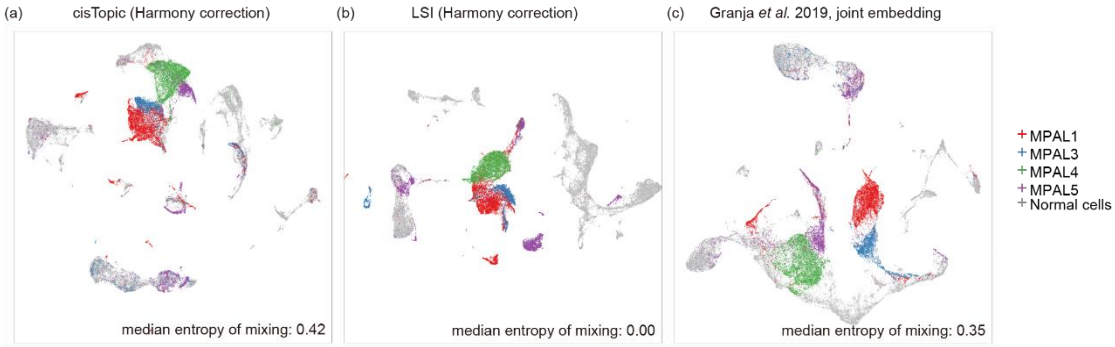

Figure S7 Benchmarking of other methods on Leukemia data. (**a**) CisTopic followed by Harmony correction. (**b**) LSI followed by Harmony correction. (**c**) Granja *et al.*'s method with joint embedding.

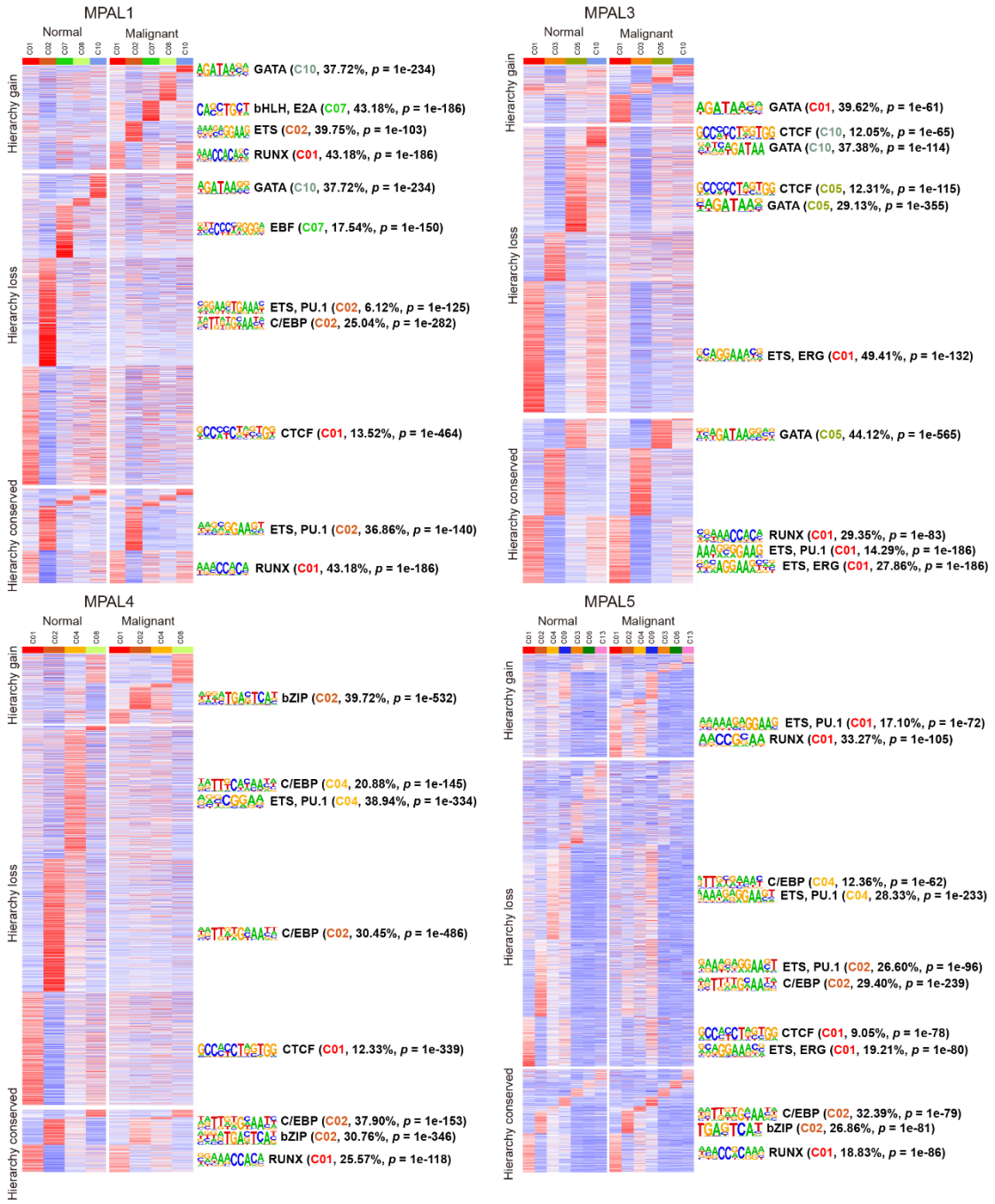

Figure S8 Aggregated ATAC-seq profiles of normal and major malignant clusters on hierarchy conserved, hierarchy loss and hierarchy gain peaks. The enriched motifs with frequency of appearance and *p*-value in each set of peaks are show in right panels.

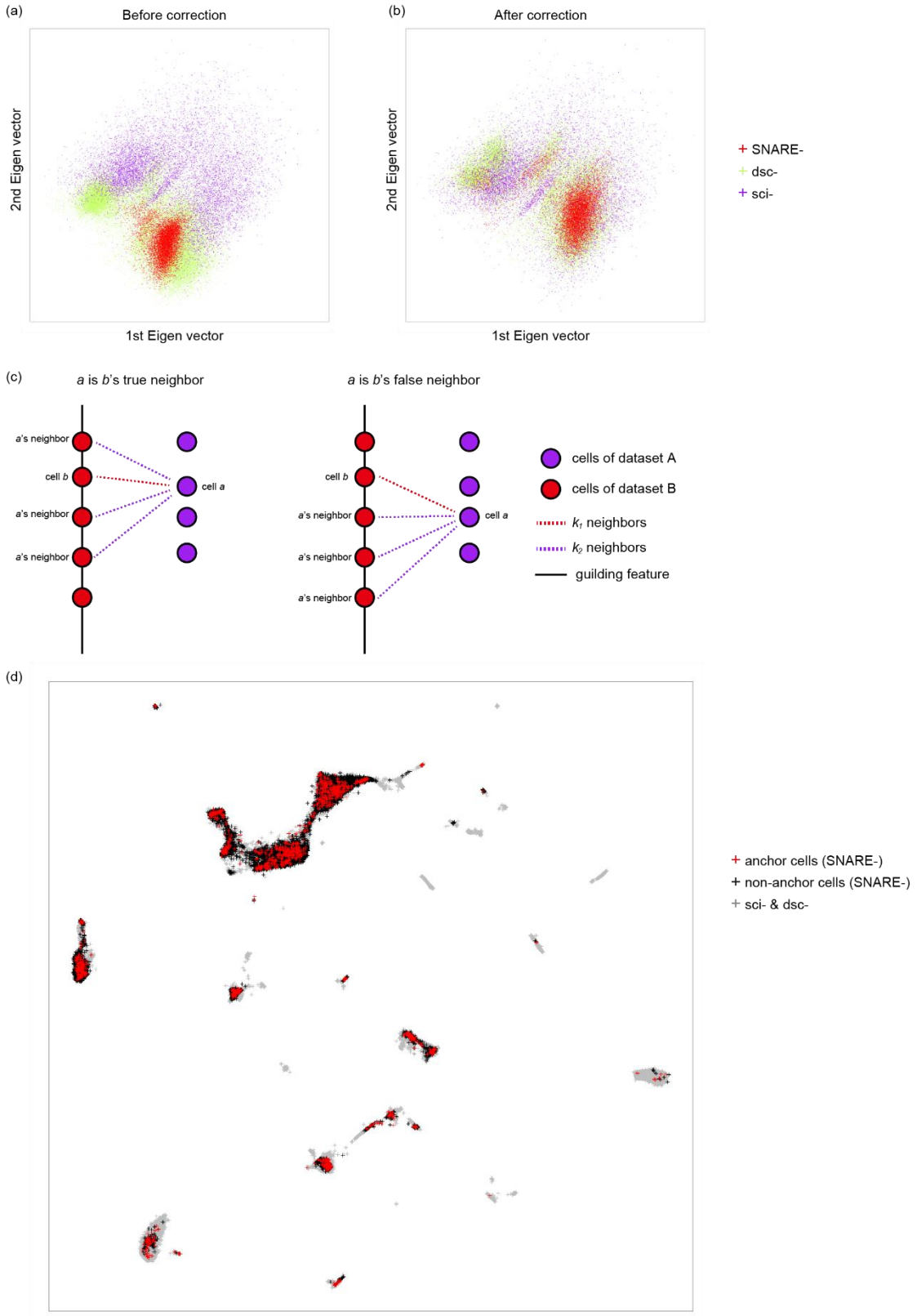

Figure S9 Algorithm details of epiConv batch correction. (**a,b**) The 1st and 2nd Eigen vectors before (**a**) and after (**b**) correction of adult mouse brain data. (**c**) Schematic view of removing false neighbors. (**d**) The distribution of anchor cells from co-assay dataset of adult mouse brain data.

534 **Table S1** Published data used in this study with running time and memory requirements

dataset	No. cells after QC	Running time (calculate similarity)	Running time (batch correction)	Memory requirement	Source
PBMCs (**Fig. 1c**)	41,909	5.5 hours	0.8 hour	< 128 GB	GSE129785 GSE123581
Adult mouse brain	53,762	7 hours	2 hours	< 256 GB	GSE126074 GSE123581 http://atlas.gs.washington.edu/mouse-atac
Developmental mouse brain	17,613	1 hour	0.5 hour	< 32 GB	GSE126074 https://support.10xgenomics.com/single-cell-atac/datasets
Leukemia	46,510	6 hours	2.1 hours	< 128 GB	GSE139369
5,000 PBMCs (**Fig. S1b**)	3,936	< 5 minutes		< 8GB	https://support.10xgenomics.com/single-cell-atac/datasets
Cell lines	1,174	< 5 minutes		<2 GB	GSE65360

535

Supplementary Note 1

Here we describe a simple method to calculate the similarities between single cells of ATAC-seq data. First, assume that we have two distributions, p_X and p_Y, where cells sample their insertion events from (the chromatin states of two types of cells). If we sample one insertion from p_X and one insertion from p_Y, we have a new random variable that is 1 if two insertions occur in the same peak or 0 otherwise. Given random binary vectors *X* with *m* non-zero elements sampled from p_X and *Y* with *n* non-zero elements sampled from p_Y, the dot product of *X* and *Y* can be considered as the sum of *m* x *n* variables and is determined by p_X and p_Y if *X* and *Y* are sparse. Thus, the $X \cdot Y/(m \cdot n)$ can be used to measure the similarity between *X* and *Y*. However, the value of $X \cdot Y$ is mainly affected by the peaks that have higher frequency. To balance the contribution of peaks with high frequency and low frequency, we weight each peak by $w = log_{10}(1 + inverse\ frequency\ of\ peak)$ following LSI, where peaks with higher frequency have lower weight. The observations from real data also support our assumption that the $X \cdot Y$ can be modeled as *m* x *n* random variables (**Fig. a** below).

In order to reduce the noise of similarity measurement, we adopt a bootstrap strategy. In *i*th bootstrap, we calculate $log_{10}\ (X_i \cdot Y_i) - log_{10}m - log_{10}n$, where we randomly sample some peaks from *X* and *Y* to generate X_i and Y_i (we sampled 20% peaks in each bootstrap and performed 15 bootstraps in this study), and use the mean of $log_{10}\ (X_i \cdot Y_i) - log_{10}m - log_{10}n$ across bootstraps as the similarity between cells.

Even after normalization by *m* x *n*, there are still some dependencies between the similarities and the library sizes. First, similarities between cells with small library sizes tends to have large variations (**Fig. b** below), which is consistent with our initial assumption as the mean value of
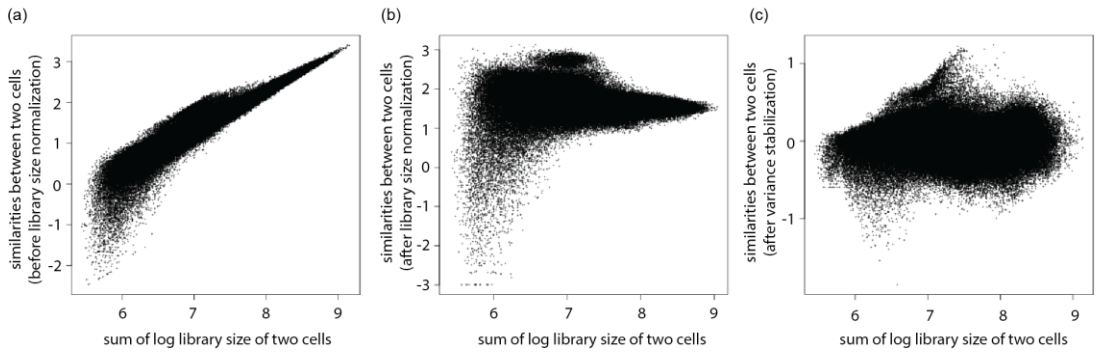
fewer random variable has larger variation. Second, there are weak negative correlation between the similarity and library size (**Fig. b** below, coefficient ≈ -0.05 in most cases), as the *m* x *n* variables are not independent. We perform linear regression on log transformed similarities and $log_{10}m + log_{10}n$. The regression residuals are further divided by the corresponding standard deviations, calculated by data points with similar $log_{10}m + log_{10}n$. The regression residuals after variance stabilization are used as the similarity scores between two cells (**Fig. c** below).